Chapter 4

InP-Based Antimony-Free MQW Lasers in 2-3 μm Band

Yi Gu and Yong-Gang Zhang

Additional information is available at the end of the chapter

http://dx.doi.org/10.5772/60705

Abstract

Mid-infrared semiconductor lasers in the wavelength range of 2-3 μm have aroused increasing interests as they are highly desired for a wide range of applications ranging from medical diagnostics to environmental sensing. Access to this wavelength range was mainly achieved by antimony-containing compound semiconductor structures on GaSb substrates. Besides, InP-based $In_xGa_{1-x}As$ (x>0.53) type-I multiple quantum well laser is a promising antimony-free approach in this band. The emission wavelength can be tailored to the 2-3 μm band by increasing the indium composition in the quantum wells. During the demonstration of this kind of lasers, controlling the strain and keeping fair structural quality is the main obstacle.

In this chapter, the route for developing this kind of lasers is reviewed. The schemes of pseudomorphic and metamorphic structures are discussed for the 2-2.5 μm and 2.5-3 μm range, respectively. In the pseudomorphic scheme, triangular quantum wells grown by digital alloy technology are applied to restrict the strain and increase the lasing wavelength. Lasers at 2.43 μm were demonstrated under continuous wave operation at room temperature. To extend the emission wavelength longer, an InP-based metamorphic template with larger lattice constant was produced and InAs quantum wells were then grown. The lasing wavelength was further increased up to 2.71 μm. The details on the gas source molecular beam epitaxial growth, device processing as well as performance characterization are presented.

Keywords: Lasers, Quantum well, InP, 2-3 μm, Antimony-free

1. Introduction

The 2-3 μm wavelength range covers both the short side of the mid-infrared (2.5-25 μm) band and the long side of the near-infrared (0.7-2.5 μm) band. Semiconductor laser diodes emitting in this spectral range are very attractive for free space communications, ultra-low loss fluoride fiber communication, solid or fiber lasers (amplifiers) pumping and seeding, light detection and ranging (LIDAR), tunable diode laser absorption spectroscopy (TDLAS), etc., due to the abundant spectroscopic features in this wavelength range. For example, the 2.1-2.4 μm band is free of water and carbon dioxide absorption as shown in Figure 1, which forms a clear atmosphere window; on the other hand, the strong and wide absorption band of water (mainly around 2.7 μm) and the moderate absorption band of carbon dioxide (around 2.0-2.1μm and 2.65-2.85 μm) forms a high contrast area, which is usable for humidity and carbon dioxide monitoring, active spectroscopic imaging of water containing subjects, etc.

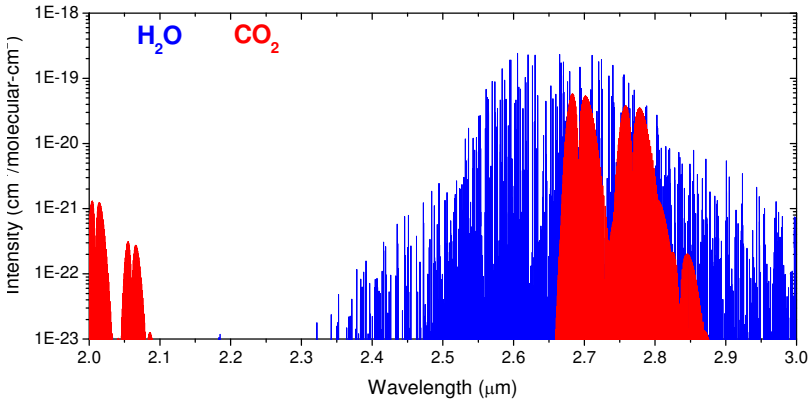

Figure 1. Absorption intensity of H_2O and CO_2 in the 2-3 μm band.

Furthermore, as shown in Figure 2, the fingerprint absorption lines of several molecules also exist in this band, and therefore, semiconductor lasers in this band are of great interest in atmospheric pollution monitoring and medical diagnostics by using TDLAS [1, 2]. As a monochromatic light source, the laser diode in this wavelength band is also desired for the evaluation of optoelectronic materials and devices such as photodetectors and focal plane arrays operated in this wavelength range, because in the measurement schemes wavelength match is very important to acquire their actual features [3, 4].

The choices and developments of semiconductor lasers in the 2-3 μm band will be reviewed at first. Then we will introduce the recent progress for the design, growth and demonstration of InP-based antimony-free multiple quantum well (MQW) lasers in this band. Schemes of pseudomorphic and metamorphic structures will be discussed for the 2-2.5 μm and 2.5-3 μm ranges, respectively.

http://dx.doi.org/10.5772/60705

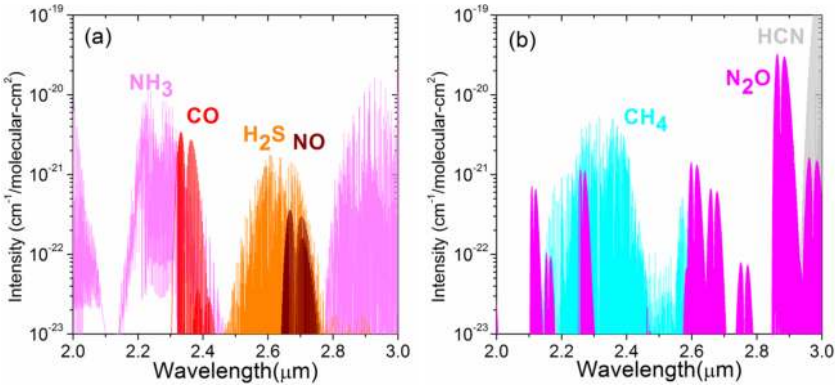

Figure 2. Absorption intensity of (a) NH_3, CO, H_2S, NO molecules and (b) CH_4, N_2O, HCN molecules in the 2-3 μm band.

2. Development of semiconductor lasers in the 2-3 μm band

There are several options of semiconductor lasers in the 2-3 μm wavelength band. Traditionally, such semiconductor lasers are developed in an antimony (Sb)-containing material system on GaSb or InAs substrates. InGaAsSb/AlGa(In)AsSb type-I quantum well (QW) lasers are the primary approach, and high power and single-mode lasers have been achieved and the wavelength range has covered 2-3.8 μm [5-10], and continuous wave (CW) operation above 80°C has been reached for 2.1 μm lasers [10]. The laser diodes have been applied in TDLAS demonstrations [11, 12]. There were also some sporadic reports on InGaAsSb/GaSb type-II QW lasers covering this band [13, 14]. GaSb-based interband cascade lasers combining type-II heterostructure and cascade concept have been developed adequately, but it is still a big challenge to shift the lasing wavelength below 3 μm, which requires new material systems [15].

Compared to GaSb, InP substrates display superior quality and are easier to acquire. Sb-containing InGaAs/GaAsSb type-II structures on InP substrates have been researched while room temperature (RT) photoluminescence (PL) and sporadic device results have been reported [16, 17]. InAsSb quantum dots (QDs) on InP are another potential scheme to demonstrate light sources in 2-3 μm, but the improvements of material quality are still needed to achieve more experimental progress [18]. On the other hand, the growth and processing technologies of the Sb-containing materials are still less mature than those of InP-based Sb-free materials. Besides, the thermal characteristics of antimonide are much inferior to the phosphides and arsenide [19, 20]. Many impressive results on mid-infrared intersubband emission of InP-based Sb-free InGaAs/InAlAs quantum cascade lasers have been reported in the recent two decades, whereas the emission wavelengths are mainly longer than 3 μm [21].

Besides the aforementioned options, InP-based Sb-free type-I $In_xGa_{1-x}As$ ($x>0.53$) QW laser is a promising approach in this band. As the bandgap wavelength of InAs at RT is as long as 3.5 μm, the emission wavelength of In(Ga)As QW can be tailored to the 2-3 μm range [22]. For this InP-based Sb-free In(Ga)As system, mature growth and processing technologies can be

relied on, and a simple structure can be applied for the type-I QW lasers using interband emission, so the laser diodes with better performance could be expected. The QW lasers applying InP-lattice-matched InGaAsP as QW layers have been well developed with the aim of telecom lasers [23]. However, the lasing wavelength is shorter than 1.7 μm. To extend the wavelength beyond 2 μm, a higher InAs composition should be applied and thus strain would be introduced into the QW layers.

The InP-based InGaAs strained QW lasers were first demonstrated by Forouhar et al. in the early 1990s [24]. The lasing wavelengths are around 2 μm at RT, and $In_{0.75}Ga_{0.25}As$ layers grown by metal-organic vapor phase epitaxy (MOVPE) were applied as the QW layers and other layers were all lattice matched to InP [25-27]. As shown in Figure 3(a), in these pseudomorphic structures, the InGaAs (x>0.53) QW layers are compressively strained whereas the other layers, such as cladding, waveguide and barrier layers, are all nearly lattice-matched to InP. The Fabry-Perot (FP) and distributed feedback buried (DFB) devices around 2.07 μm were then demonstrated by NTT's group [28-31]. After the year 2000, FP and vertical-cavity surface-emitting lasers (VCSELs) at 2.3 μm were demonstrated by Amann et al. using molecular beam epitaxy (MBE) grown InAs-containing triangular QW active region [32-34]. Using MOVPE grown 5 nm pure InAs as the QW layer, Mitsuhara et al. in NTT's group reported FP and DFB lasers with lasing wavelength at 2.33 μm [35-37]. Lasers up to 2.4 μm were recently demonstrated by using triangular QWs grown by MBE digital alloy technology [38].

As mentioned earlier, further increase of well width is restrained by the strain between the QW part and InP substrate, and thus the longest emission wavelength is limited. To extend the emission wavelength to longer wavelengths, a metamorphic "virtual substrate" can be produced with a larger lattice constant than InP, e.g. metamorphic $In_{0.8}Ga_{0.2}As$ layer as shown in Figure 3(b). In this case, the critical thicknesses can be larger than those of pseudomorphic structures, therefore the QW width can be increased, which would increase the emission wavelength. Recently, step-graded $InAs_xP_{1-x}$ buffers on InP have been applied to achieve 2.8-3 μm PL at RT [39-41], where 16.5 nm InAs or 22 nm $InAs_{0.94}P_{0.06}$ were used as the well layers. By using 15 nm InAs QWs on continuously-graded metamorphic $In_xAl_{1-x}As$ buffers, RT PL of QWs at 3.05 μm [42] and low temperature lasing of laser diodes at 2.7 μm have been achieved [43]. This scheme can even be explored to mid-infrared metamorphic InAs QWs on GaAs substrate, which is even more attractive than on InP substrate [44].

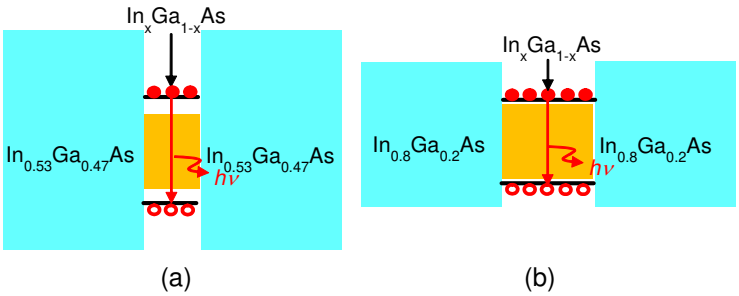

Figure 3. Schematic diagrams of the transition for the InP-based (a) pseudomorphic and (b) metamorphic $In_xGa_{1-x}As$ QWs.

http://dx.doi.org/10.5772/60705

3. Theoretical evaluation of InP-based Sb-free type-I QW lasers

At first, we theoretically evaluate the type-I transition energy and emission wavelength of rectangular pseudomorphic $In_xGa_{1-x}As/In_{0.53}Ga_{0.47}As$ (x>0.53) and metamorphic $In_xGa_{1-x}As/In_{0.8}Ga_{0.2}As$ (x>0.8) QWs. The subband energies of the QWs were calculated by numerically solving the Schrödinger equation with strain-contained 4×4 Luttinger-Kohn Hamiltonian, and the transition energy from the first electron energy level to the first heavy hole energy level was calculated. The emission wavelength versus the well width of $In_xGa_{1-x}As/In_{0.53}Ga_{0.47}As$ (x>0.53) and $In_xGa_{1-x}As/In_{0.8}Ga_{0.2}As$ (x>0.8) QWs are shown in Figure 4(a) and Figure 4(b), respectively. The well width is limited by the critical thickness calculated from the force balance model as shown in Figure 4. It is seen that the critical thickness can be extended by using the metamorphic scheme, and therefore, a thicker well width can be used, leading to a longer wavelength.

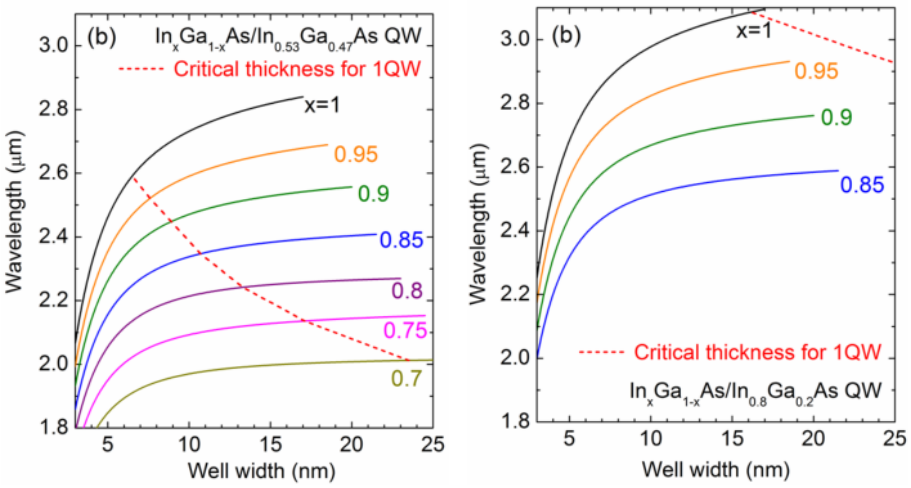

Figure 4. Calculated transition wavelength versus well width of (a) pseudomorphic $In_xGa_{1-x}As/In_{0.53}Ga_{0.47}As$ QW (x>0.53) and (b) metamorphic $In_xGa_{1-x}As/In_{0.8}Ga_{0.2}As$ QW (x>0.8) with rectangular QW shape. The critical thickness for a single QW is indicated as the dotted line.

Furthermore, calculation shows that the lasing wavelength can be extended dramatically if the energy band shape is changed from a rectangular to a triangular one [45, 46]. Figure 5(a) shows the schematic band structure of the $InAs/In_{0.53}Ga_{0.47}As$ triangular QW (TQW) and $In_{0.765}Ga_{0.235}As/In_{0.53}Ga_{0.47}As$ rectangular QW (RQW). The two QW structures are considered to have the same strain extent in the QW part. From Figure 5(b), we can see that changing the energy band from the rectangular shape to a triangular one redshifts the lasing wavelength markedly. For the well width of 16 nm, the calculated wavelength of RQW is only about 2.1 μm, but it is beyond 2.5 μm for TQW. The theoretical estimations show the promising potential of the TQW to extend the wavelength and improve the performances.

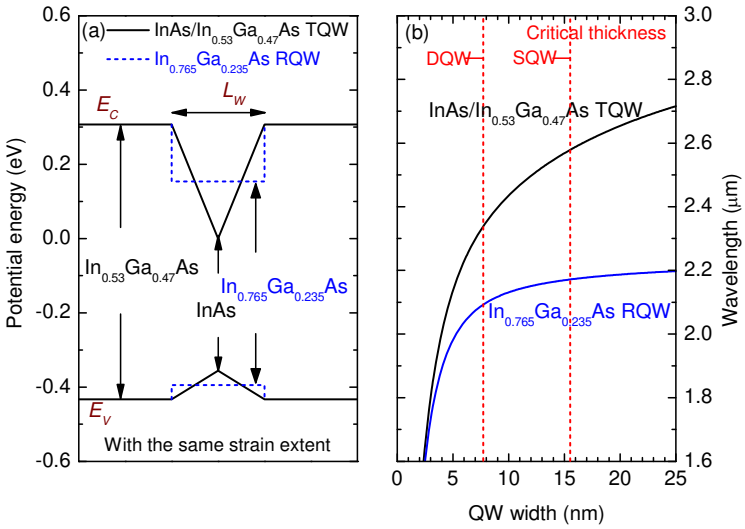

Figure 5. (a) Schematic band structures and (b) calculated transition wavelength as a function of well width of InAs/$In_{0.53}Ga_{0.47}As$ TQW and $In_{0.765}Ga_{0.235}As/In_{0.53}Ga_{0.47}As$ RQW with the same strain extent. The critical thicknesses for single QW and double QWs are indicated.

4. Pseudomorphic scheme for lasing wavelength below 2.5 μm

The pseudomorphic scheme is based on the lattice-mismatched material system except the active QW region. Therefore, the main concern of such lasers is the control of strain in the QW and to keep fair structural quality. The gas source molecular beam epitaxy (GSMBE) growth parameters and the structures of the QW parts need to be optimized at first [47, 48]. Then the whole laser structures were grown and the lasers were demonstrated and analyzed.

4.1. GSMBE growth and optimization of pseudomorphic triangular QWs

To construct the QWs with triangular shape in practice, usually two methods can be applied. The first one uses analogue alloy where the emission source flux changes gradually with an extremely low rate [49], and the other one uses the so-called digital alloy, where short period superlattice composed of two materials are grown at digitally setting thicknesses [50]. The growth rate is normal for the latter one, and this method is especially much more convenient for molecular beam epitaxy (MBE). In MBE, the time for opening and closing a shutter is far below 1 s, so the control precision of the short period superlattice can be high enough. It is also found that digital alloy technology can extend the critical thickness and restrain the three-dimensional material growth [51, 52].

A VG Semicon V80H GSMBE system was applied for the growth. The best background vacuum achieved in this system was about 1×10^{-11} Torr. The elemental indium and gallium cells with

http://dx.doi.org/10.5772/60705

two heaters as well as aluminum standard cell were used as group III sources. The fluxes of these group III emission sources were controlled by the cell temperatures. Group V sources were As_2 and P_2 cracked from Arsine (AsH_3) and phosphine (PH_3) cracking cells at around 1000 °C. The fluxes of As_2 and P_2 were controlled by pressure. Standard beryllium and silicon cells were used as *p*- and *n*-type doping sources, respectively. The doping levels were controlled by the temperatures of the emission cells. The growth rates of InP-lattice-matched InGaAs(P) and InP layers were all controlled to be around 1 μm/h.

Sample	Designed			T_g (°C)	Parameters from HRXRD simulation		PL wavelengths (μm)		PL FWHM (meV)	
	λ_{300} (μm)	d_W (nm)	d_B (nm)		d_W (nm)	d_B (nm)	300 K	12 K	300 K	12 K
1	2.1	9	15	500	9.1	16.2	2.14	1.94	35	24
2	2.1	9	15	530	9.1	16.4	2.11	1.93	35	19
3	2.3	13	15	530	14.0	16.4	2.25	2.07	31	20
4	2.5	19	15	530	19.2	16.4	2.38	2.16	36	24
5	2.5	19	20	530	19.2	20.6	2.38	2.16	33	17
6	2.6	25	20	530	N/A	N/A	N/A	2.26 & 2.31	N/A	24 & 31

Table 1. The structure, growth parameters, HRXRD and PL results of the samples. λ_{300} is the wavelength at 300 K, T_g is the growth temperature, d_W and d_B is well width and barrier width, respectively.

The grown QW samples consisted of a 200-nm-thick InP buffer layer, two triangular QWs and a 100-nm-thick InP cap layer. The triangular QWs were constructed by growing InGaAs/InAs digital alloy with very short periods. In each period the thicknesses of $In_{0.53}Ga_{0.47}As$ (d_1) and InAs (d_2) is designed from the following equation:

$$\begin{cases} \left(d_1 \times 0.53 + d_2\right)/d = \alpha \\ d_1 + d_2 = d \end{cases} \tag{1}$$

where α is the expected average indium composition in each short period, and d is the period of the short period setting to be 1 nm here. The barrier layer is AlInGaAs grown using the growth parameters of InP-lattice-matched $In_{0.52}Al_{0.48}As$ and $In_{0.53}Ga_{0.47}As$, thus the composition is around $Al_{0.33}In_{0.36}Ga_{0.31}As$.

Table 1 lists the structure parameters, growth conditions, high resolution X-ray diffraction (HRXRD) and PL results of the grown QW samples. The HRXRD (004) scanning curves of all samples are shown in Figure 6. For all the samples, the upper and lower curves show the measured and simulated results, respectively. The good agreement between the measurement and simulation in samples 1-5 indicates the pseudomorphic growth. By simulation, the average indium composition in the well and barrier layers were about 0.765 and 0.355 in samples 1-5,

the deduced well widths d_w and barrier widths d_B for all the samples are also listed in Table 1, agreeing well with the designed values. Figure 7 presents the PL spectra of samples 1-6 at RT and 12 K, respectively. The peak wavelengths and full-width at half-maximum (FWHM) of the PL spectra are listed in Table 1.

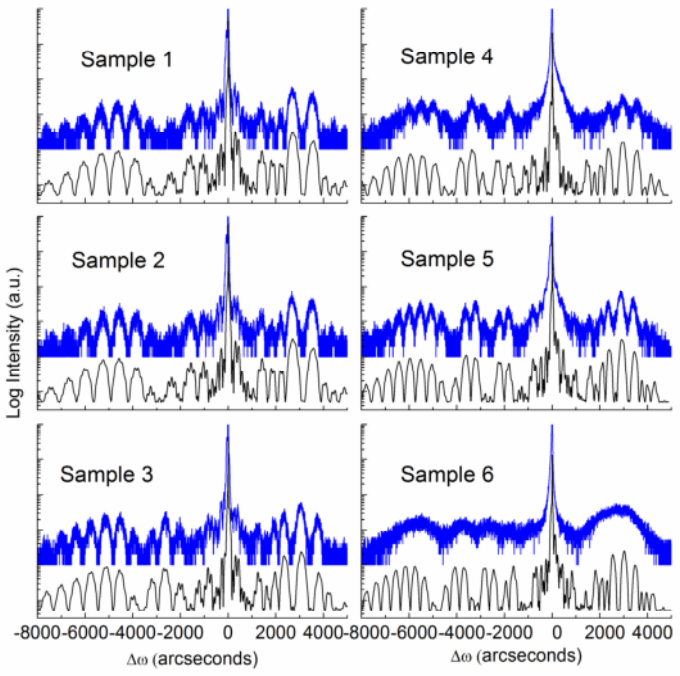

Figure 6. HRXRD (004) scanning curves of the TQWs with various structures and growth parameters [48]. (Reprinted with permission from Elsevier)

The growth temperature T_g is a crucial growth parameter for high crystalline and optical quality during the MBE growth. For the growth of high indium materials, generally T_g needs to be lowered. However, for the $In_{0.53}Ga_{0.47}As$ barriers and the Al-containing AlInGaAs barriers, a relatively higher growth temperature is preferred to improve the optical properties. It is really unpractical to increase and decrease T_g in the interface of well and barrier layers, because the interface quality would be significantly deteriorated by the growth interruption. Therefore, T_g is needed to be optimized, especially for the QW growth. Samples 1 and 2 are with different growth temperatures at 500 °C and 530 °C, respectively. Figure 6 shows the sharp satellite peaks in the HRXRD scanning curves of samples 1 and 2, denoting the nice crystalline quality of both samples. Similarly, PL spectra of the two samples have been observed at 300 K as shown in Figure 7, whereas at 12 K the PL intensity of sample 2 is stronger than that of sample 1. The FWHM at 12 K is 19 meV for sample 2, and 24 meV for sample 1. It is shown that the sample grown at a relatively higher temperature shows better optical quality.

http://dx.doi.org/10.5772/60705

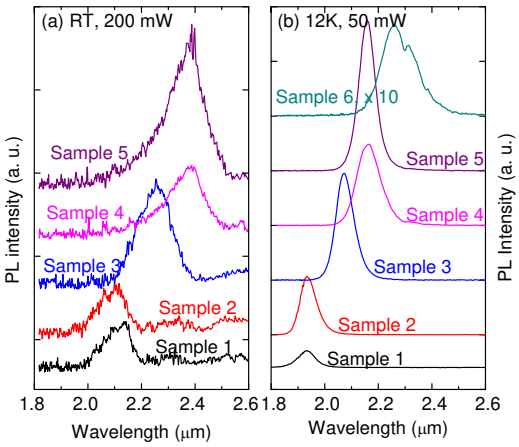

Figure 7. PL of triangular QWs with various structures and growth parameters at RT and 12 K [48]. (Reprinted with permission from Elsevier)

By increasing the well width from 9 nm of sample 2 to 13 nm of sample 3 and 19 nm of sample 4 while keeping the same barrier width, the HRXRD curve becomes indistinct as shown in Figure 6, indicating the deteriorated crystalline quality of sample 4. As the QW width increases, more defects may be generated due to the larger lattice mismatch. The wider QW also weakens the quantum restriction, and the carriers have more probability to occupy the second subband, which induces the larger PL FWHM and the much shorter peak wavelength than designed for sample 4. For sample 5, by increasing the barrier width on the basis of sample 4, the satellite peaks of HRXRD curves recover to be distinct and the PL intensity is enhanced. The PL FWHM is reduced to 17 meV at 12 K and 33 meV at 300 K for sample 5, comparing to 24 meV at 12 K and 36 meV at 300 K for sample 4. The well width of sample 6 is further enlarged to 25 nm in order to extend the wavelength further. It can be seen from Figure 6 that the satellite peaks of the HRXRD curve become indistinct, and two PL peaks at 12 K exist as shown in Figure 6(b), whereas no PL signal is observed at 300 K. It suggests that 2.4 μm is around the ceiling wavelength for the In(Ga)As strained QW.

4.2. Demonstration of CW-operated lasers above room temperature

In our preliminary work, InP layers were applied as waveguides for the convenience of the growth, but the lasing could only be achieved below 150 K [53, 54]. Subsequently, InGaAsP quaternary alloys with bandgap around 1.1 eV and lattice-matched to InP were used as the waveguide layers, and the laser performances were dramatically improved. In this section, the performances of RQW and TQW lasers at 2.2 μm will be presented. And the demonstration of TQW lasers beyond 2.4 μm with increased QW width will also be introduced.

For the lasers with designed lasing wavelength at 2.2 μm, two structures with RQW and TQW were grown [52]. The active QW regions of both samples were sandwiched between 120-nm-

thick InGaAsP waveguide layers, as well as 1000-nm-thick *n*-type bottom and 1700-nm-thick *p*-type upper InP cladding layers, and 300-nm-thick p-type $In_{0.53}Ga_{0.47}As$ layers were grown as a top contact layer. The active QW region was formed by four QW layers sandwiched between 20-nm-thick $In_{0.53}Ga_{0.47}As$ barriers for both samples. The QW layers were 3-nm-thick compressive InAs layers in the RQW structure, and 10-nm-thick triangular $In_{0.53}Ga_{0.47}As$/InAs/$In_{0.53}Ga_{0.47}As$ layers in the TQW structure. The total strain content of the TQW was still larger than that of the RQW due to the much thicker well width.

Ridge waveguide lasers with a strip width of 6 μm were fabricated by standard lithography and wet chemical etching process. Then, a 300-nm-thick Si_3N_4 layer was deposited by using plasma enhanced chemical vapor deposition (PECVD). On the top of the ridge a 4-μm-wide window was opened. The top and bottom metallic contacts were sputtered Ti/Pt/Au and evaporated Ge/Au/Ni/Au, respectively. The chips were cleaved into 0.8-mm-cavity-length bars with uncoated facet, soldered on copper heat sinks and wire bonded.

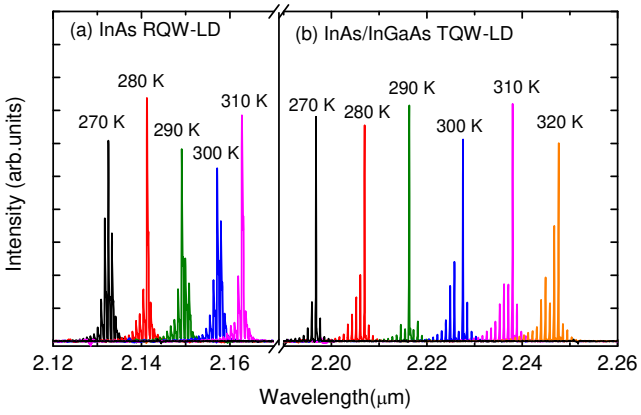

Figure 8. Lasing spectra of (a) rectangular QW laser and (b) triangular QW laser around 2.2 μm at various temperatures under CW driving condition.

Figure 8 shows the CW lasing spectra at a driving current of 1.2 times the threshold current in a temperature step of 10 K. The maximum operation temperature of the RQW laser is about 310 K and the lasing peak is about 2.16 μm at 310 K, whereas the TQW laser shows an increased maximum operation temperature up to 330 K. Over the whole temperature range, the lasing peaks of the TQW laser are about 60 nm longer than those of the RQW laser, probably due to the model error in theoretical design as well as due to the growth error. These results show that the TQW laser can operate at higher temperatures even with a longer lasing wavelength, proving the benefit of TQW. The average temperature coefficient of the lasing wavelength $\Delta\lambda/\Delta T$ is about 0.8 nm/K for the RQW laser and 1 nm/K for the TQW laser.

The temperature-dependent I-P characteristics and the I-V curve at 300 K of the lasers are shown in Figure 9. The threshold current of the RQW laser is 124 mA at 300 K, corresponding

http://dx.doi.org/10.5772/60705

to a threshold current density of 2.58 kA/cm^2, and the output power is 3.6 mW/facet at an injection current of 400 mA. In contrast, the TQW laser shows a much lower threshold current of 68 mA (1.42 kA/cm^2) at 300 K. Also, a much higher output power of 10.4 mW/facet is obtained at 300 K, almost three times that of the RQW laser. The turn-on voltage and the differential resistance for both lasers are almost the same at about 1.25 V and 1.87 Ω at 300 K.

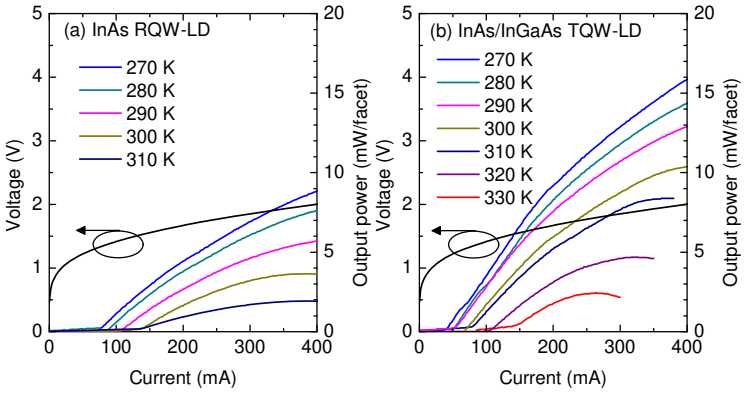

Figure 9. I-P and I-V characteristics of (a) rectangular QW laser and (b) triangular QW laser around 2.2 μm at various temperatures under CW driving condition.

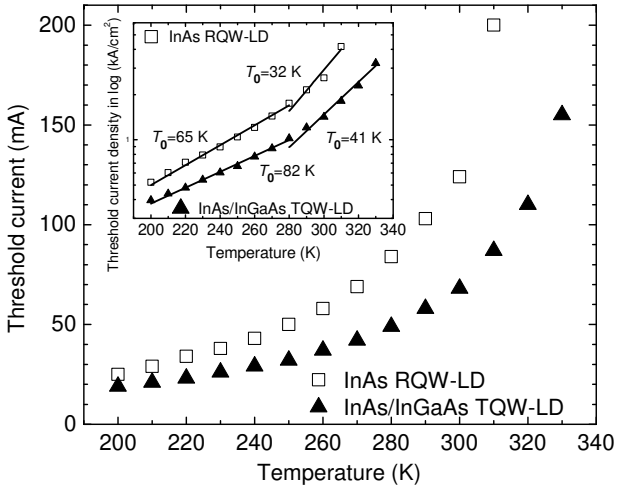

Figure 10. Temperature-dependent threshold current of rectangular QW laser and triangular QW laser around 2.2 μm at various temperatures under CW driving condition. The inset shows the temperature-dependent threshold current densities and characteristics temperatures.

The threshold current as a function of temperature is shown in Figure 10, covering the temperature range from 200 K to 310 K and 330 K for the RQW and TQW lasers, respectively. The characteristic temperatures were achieved from the temperature-dependent threshold current density as shown in the inset of Figure 10. In the low temperature range 200-280 K, a characteristic temperature of T_0=82.1 K was obtained for the TQW laser, higher than the value of T_0=65.2 K for the RQW laser. In the high temperature range beyond 290 K, T_0 is decreased for both lasers, but the TQW laser also has a higher value of T_0=40.5 K than the T_0=32.1 K for the RQW laser.

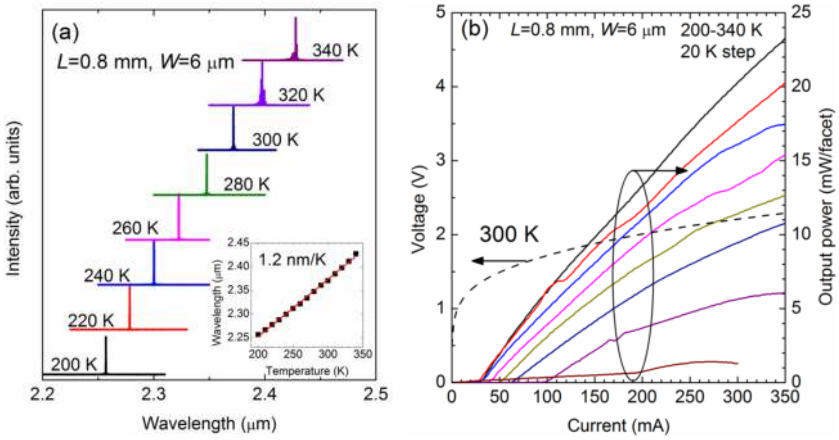

Figure 11. (a) The CW lasing spectra of the around 2.4 μm TQW laser at various temperatures. The inset shows the temperature-dependent lasing wavelength. (b) Output power at different temperatures and voltage at 300 K as a function of injected current of the around 2.4 μm TQW laser [38]. (Copyright 2014 The Japan Society of Applied Physics)

By further increasing the well width of TQW laser to 16 nm, the lasing wavelength of the device has been extended. Figure 11(a) shows the CW lasing spectra in the temperature range of 200 K to 340 K. The lasing wavelength is 2.37 μm at 300 K and red-shifts to 2.43 μm at 340 K. The average temperature coefficient of the wavelength is 1.2 nm/K in 200-340 K as shown in the inset of Figure 10(a). As shown in Figure 11(b), the output power at 200 K in CW mode is 23 mW/facet injected by a current of 350 mA and at 300 K the power dropped to around 11 mW/facet. At 200 K the threshold current is 24 mA and at 300 K the threshold current is increased to 62 mA. The corresponding threshold current density is 1.3 kA/cm^2 for the laser with four QWs and 325 mA/cm^2 for each QW, respectively. At 340 K the maximum output power is decreased to 1.4 mW/facet with a threshold current of 186 mA.

The laser threshold current density and external differential quantum efficiency η_d as a function of temperature are shown in Figure 12(a). The characteristic temperature T_0 is derived to be about 99 K in the temperature range of 200-300 K, and decreases to 35 K in 300-340 K range. The external differential quantum efficiency at 200 K is 41% and is decreased to 23% at 300 K and is further dropped to 7% at 340 K. The quantum efficiency characteristic temperature of T_1=142 K is obtained by fitting the external differential quantum efficiency in 200-320 K temperature range.

http://dx.doi.org/10.5772/60705

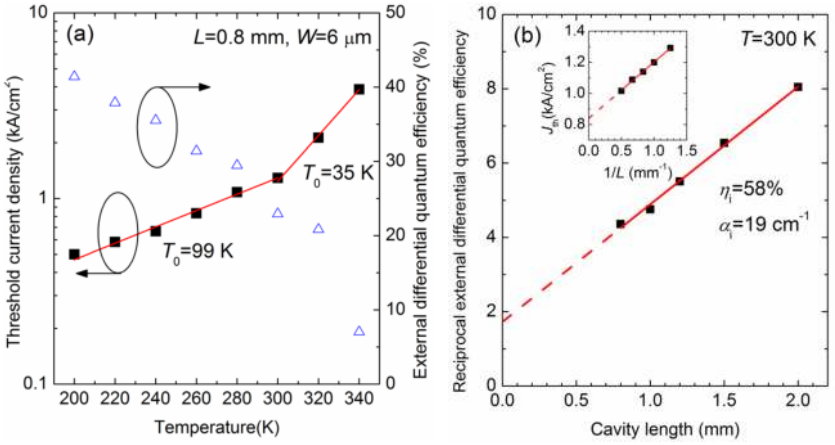

Figure 12. (a) Temperature dependence of the threshold current density and external differential quantum efficiency of the 2.4 μm TQW laser. The lines are the fitting lines of threshold current density in two temperature ranges. (b) Reciprocal external differential quantum efficiency of the TQW lasers as a function of the cavity length at 300 K. The inset shows the threshold current density (J_{th}) versus the reciprocal cavity length ($1/L$). The solid lines are the fitting of the measured data, and the dashed lines are the extrapolated data [38]. (Copyright 2014 The Japan Society of Applied Physics)

The reciprocal external differential quantum efficiency η_d as a function of the cavity length is shown in figure 12(b). The internal quantum efficiency η_i and internal loss α_i are calculated by fitting the data following $1/\eta_d=(1/\eta_i)[1+\alpha_i L/\ln(1+R)]$, where L is the cavity length and R is the facet reflectivity. Taking R as 0.35 for the as-cleaved facet in the calculation, the internal quantum efficiency and internal loss is calculated to be 58% and 19 cm^{-1}, respectively. Note that the internal quantum efficiency value is favorable but the loss is relatively high, which limits the laser performances. The intervalence band absorption in the *p*-type InP up cladding is one main cause of the large internal loss. The inset of Figure 11(b) illustrates the threshold current density versus the reciprocal cavity length. By extrapolation, the threshold current density at infinite cavity length is 841 A/cm^2 (210 A/cm^2 per QW).

5. Metamorphic scheme for lasing wavelength beyond 2.5 μm

For the metamorphic scheme, InAlAs graded buffers were grown on InP substrate to form the metamorphic template with larger lattice constant than InP. The InAs QW structures were then grown on the template with thicker QW width, and the wavelength could be beyond 2.5 μm. For this kind of metamorphic laser structures, the material quality is very crucial for the device performance, therefore both of the buffer layers and growth parameters were optimized to improve the buffer quality. On the basis of the buffer optimization, the lasers were grown, demonstrated and characterized.

5.1. GSMBE growth and optimization of metamorphic buffers and QWs

As a preliminary experiment, the metamorphic buffer composed of a 2.5-μm-thick $In_xAl_{1-x}As$ continuously graded buffer and a 1-μm-thick $In_{0.8}Ga_{0.2}As$ virtual substrate layer were grown on InP substrate after the growth of a 100-nm-thick InP buffer layer. In the graded buffer, the indium composition x was graded from 0.52 to 0.8 through the simultaneously linear increase of indium source temperature and decrease of aluminum source temperature. After that, two periods of InAs/$In_{0.53}Ga_{0.47}As$ strained QWs were grown. The $In_{0.53}Ga_{0.47}As$ barrier is used to compensate the compressive strain of InAs well comparing to the virtual substrate layer. The lattice mismatch of InAs well and $In_{0.53}Ga_{0.47}As$ barrier with respect to $In_{0.8}Ga_{0.2}As$ virtual substrate layer is +1.3% and -1.8%, respectively. Two samples were grown and the widths of InAs well and $In_{0.53}Ga_{0.47}As$ barrier were 10 nm/7 nm and 15 nm/10 nm, respectively to form a strain compensated QW structure with minimal residual strain. The $In_{0.53}Ga_{0.47}As$ barrier can also stop the diffusion of exited carriers between the QW region and the rest part of the sample.

The grown samples show mirror-like surface morphology without haziness under optical microscopy. Regular cross-hatch patterns are observed on the surfaces with ridges and troughs along the [110] and [1-10] crystal directions. The root mean square (RMS) roughness measured by atomic force microscope (AFM) over 40×40 μm^2 is 3.9 nm and 6.1 nm for the 10 nm and 15 nm QW lasers, respectively. From the cross-sectional transmission electron microscope (XTEM) images of 15 nm QW laser measured at 160 kV as shown in Figure 13, the dislocations are mainly localized within the $In_xAl_{1-x}As$ graded buffer and do not propagate into the upper structures. The $In_{0.8}Ga_{0.2}As$ virtual substrate layer is free of dislocations in the XTEM measurements, which means the threading dislocation density is under the detection limit (about 10^7 cm^{-2}). In the amplificatory image of the InAs/$In_{0.53}Ga_{0.47}As$ QWs region, distinct interfaces between the well and barrier layers are observed. The thickness fluctuations of wells and barriers are revealed around ±1 nm by a careful inspection.

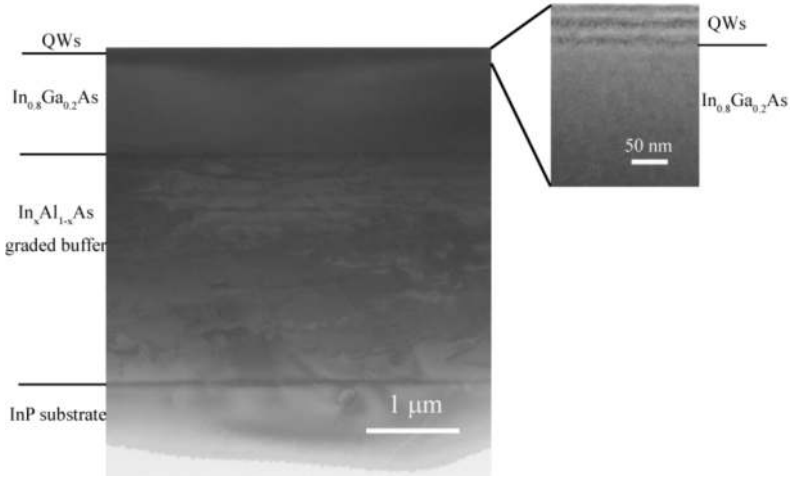

Figure 13. Bright-field XTEM images of the InP-based metamorphic QW epitaxy structure [42]. (Reprinted with permission from AIP)

http://dx.doi.org/10.5772/60705

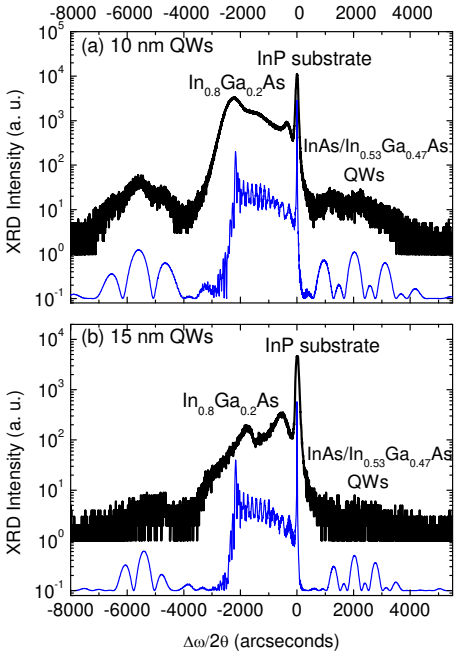

Figure 14. HRXRD (004) scanning curves of InP-based metamorphic (a) 10 nm QWs and (b) 15 nm QWs. The thick and thin lines show the measured and simulated results, respectively [42]. (Reprinted with permission from AIP)

The HRXRD ω/2θ (004) scanning curves were measured and shown in Figure 14 (thick lines). The peak with the largest intensity corresponds to InP substrate, and the wide peak with a relaxed mismatch of 1.8×10^{-2} with respect to InP corresponds to $In_{0.8}Ga_{0.2}As$ virtual substrate layer. The HRXRD signals from the virtual substrate of the two samples show some difference, but become the same after etching away the QW regions at surface. Rough satellite peaks, related to the InAs/$In_{0.53}Ga_{0.47}As$ QWs, are observed symmetrically on the both sides of the $In_{0.8}Ga_{0.2}As$ peak, indicating the strain compensation effect with respect to the $In_{0.8}Ga_{0.2}As$ virtual substrate layer. The lattice dynamical simulations were also performed and the simulated curves are shown in Figure 14 (thin lines). In the simulation, the thicknesses of the wells/barriers were set the same as the design. The $In_xAl_{1-x}As$ buffer was assumed graded relaxed and the $In_{0.8}Ga_{0.2}As$ virtual substrate layer fully relaxed with respect to InP substrate, meanwhile InAs wells and $In_{0.53}Ga_{0.47}As$ barriers were fully strained with respect to $In_{0.8}Ga_{0.2}As$ virtual substrate layer.

The PL measurements were performed as shown in Figure 15. The photo-excited carriers are very sensitive to threading dislocations due to the diffusion length of photo-excited carriers in micrometers. Therefore, the PL intensity can reflect the material quality. The strong PL intensity at 300 K in Figure 15(a) indicates few threading dislocations in QW structures. For each sample, two emission peaks can be observed at 300 K, where the peak at about 2.4 μm corresponds to $In_{0.8}Ga_{0.2}As$ virtual substrate layer, the peaks at 2.90 μm and 3.05 μm for the

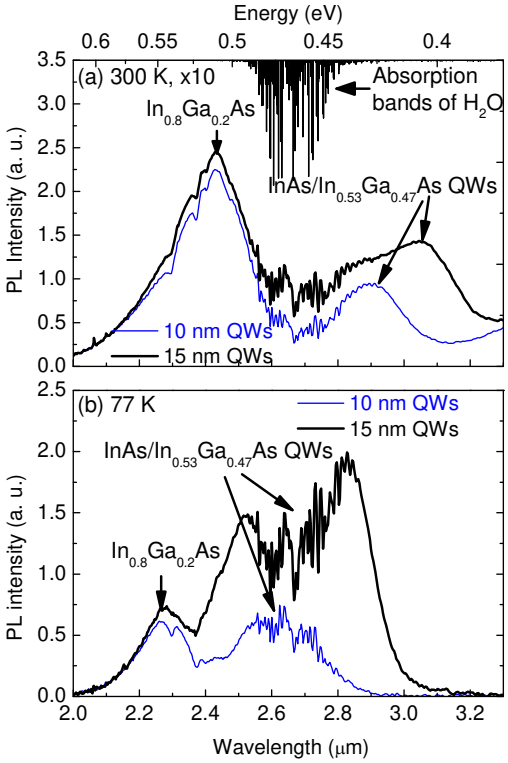

Figure 15. PL results of the metamorphic QW samples at (a) 300 K and (b) 77 K. The thin and thick lines show the results of 10 nm and 15 nm QWs, respectively. The absorption bands of water are also indicated [42]. (Reprinted with permission from AIP)

two samples correspond to the active QWs. In Figure 15(b) the peak corresponds to $In_{0.8}Ga_{0.2}As$ buffer blue-shifts to about 2.3 μm at 77 K. The PL signals of active QWs blue-shift to about 2.6 μm and 2.7 μm at 77 K for the 10 nm and 15 nm QW lasers, respectively, and the peak shapes are affected significantly by the water absorption. The relatively wide PL peaks even at low temperatures are possibly due to the presents of lattice defects and the poor carrier confinement on the top side of the QW. The metamorphic QWs with 15 nm thick InAs layer still show moderate optical quality. This structure is promising for the lasers around 3 μm.

5.2. Demonstration of metamorphic CW-operated lasers at low temperatures

To demonstrate the metamorphic lasers, the effects of strain-compensated QWs and separate confinement heterostructure (SCH) were studied. The growth of the samples started with a 200-nm-thick n^+ InP buffer layer grown, followed by a 1800-nm n^+ $In_xAl_{1-x}As$ continuously graded buffer layer, both highly doped with Si to about 2×10^{18} cm^{-3}. In the graded buffer the indium composition was graded from 0.52 to 0.84 introducing an indium composition

http://dx.doi.org/10.5772/60705

overshoot of 0.04 to achieve the full relaxation of the metamorphic layer. Then an 800-nm n^+ $In_{0.8}Al_{0.2}As$ cladding layer with carrier density of about 2×10^{18} cm^{-3} was grown to form a template. Then a 150-nm-thick n^- waveguide layer, undoped active double QWs and a 150-nm-thick p^- waveguide layer were grown [55]. The schematic band energy of the active regions for samples A, B and C can be found in Figure 16, where the solid lines indicate samples A and B whereas the dotted lines indicate sample C. For sample A $In_{0.8}Al_{0.2}As$ was used as the waveguide layers, which was the same as the cladding layers. For samples B and C, $In_{0.8}Ga_{0.2}As$ was used as the waveguide layers so that the SCH consisting of $In_{0.8}Ga_{0.2}As$ waveguide and $In_{0.8}Al_{0.2}As$ cladding layers were constructed. In the double QW region, a strain-compensated structure was used for sample A, formed by two 12-nm InAs wells sandwiched by $In_{0.6}Ga_{0.4}As$ barriers with the strains of +1.4% and -1.4% with respect to the $In_{0.8}Al_{0.2}As$ template. On the other hand, $In_{0.8}Ga_{0.2}As$ was used as the barrier layers in sample B, thus no strain compensation was applied in the QW region. Sample C combined the SCH and strain-compensated QWs, where 15-nm-thick InAs well and 15-nm-thick $In_{0.6}Ga_{0.4}As$ barrier layers were applied. At last, a 1700-nm-thick p^+ $In_{0.8}Al_{0.2}As$ cladding layer and a 300-nm-thick p^+ $In_{0.8}Ga_{0.2}As$ contact layer were grown, heavily doped with Be to higher than 5×10^{18} cm^{-3}.

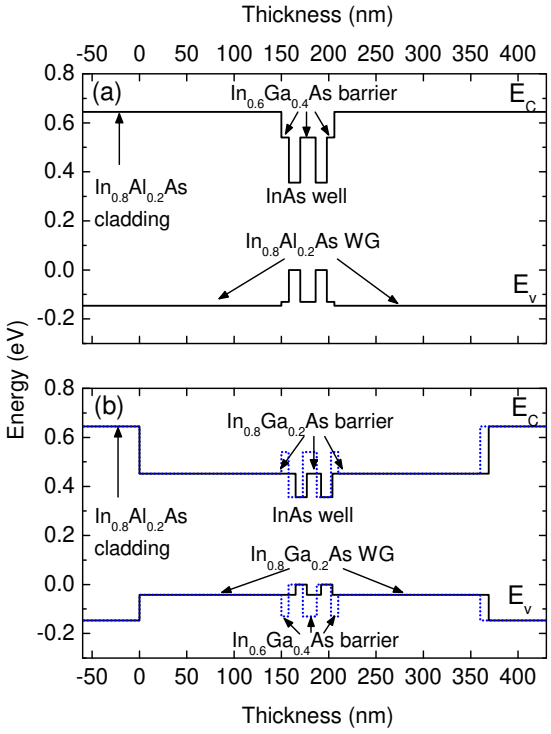

Figure 16. Schematic energy-band diagrams of the active regions of (a) sample A, (b) sample B (solid line) and sample C (dotted line) [55]. (Reprinted with permission from IOP)

Figure 17 shows the HRXRD scanning curves and PL spectra of the samples after etching away the p-type contact layer and p^+ $In_{0.8}Al_{0.2}As$ cladding layer. Rough satellite peaks, related to the QWs, can be observed on the left side of the $In_{0.8}Al_{0.2}As/In_{0.8}Ga_{0.2}As$ peaks for the samples, although they are not so distinct. Comparing the intensities of $In_{0.8}Al_{0.2}As/In_{0.8}Ga_{0.2}As$ and QW peaks for the three samples, it is observed that the layer peak intensities of samples A and C with strain-compensated QWs are stronger than those of sample B without strain compensation. The lattice dynamical simulations were also performed and the HRXRD intensities of layer peaks on the left side of InP substrate were very close for all the samples in the simulations. Therefore, the measured stronger layer peak intensities of samples A and C indicate their better material quality than sample B due to the strain compensation of QW regions.

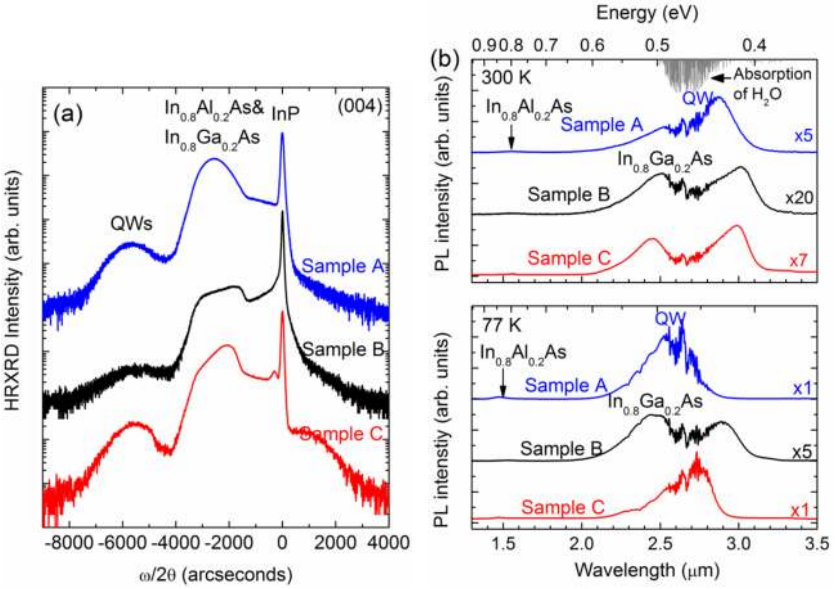

Figure 17. (a) HRXRD ω/2θ scanning curves of the QW lasers on InP-based metamorphic InAlAs buffers. (b) PL emissions of the QW structures on InP-based metamorphic InAlAs buffers at 300 K and 77 K [55]. (Reprinted with permission from IOP)

As shown in Figure 17(b), the PL signals between 2.6-2.8 μm are affected by the absorption of water vapor. Two PL peaks are observed for sample A, the relatively weak peak at 1.55 μm corresponds to the $In_{0.8}Al_{0.2}As$ cladding and waveguide layers, and the peak at 2.88 μm corresponds to the QWs. For sample B, there are also two PL peaks, and the PL signal of $In_{0.8}Al_{0.2}As$ is not clear in linear scale. The two PL peaks at 2.51 μm and 3.02 μm correspond to $In_{0.8}Ga_{0.2}As$ waveguide layers and the QWs, respectively. The PL intensities of the QWs for samples A and C are several times of that of sample B at both 300 K and 77 K, confirming the better material quality of samples A and C. The phenomenon of PL measurements is consistent with the results of HRXRD.

The ridge waveguide lasers were then demonstrated and the cross-section of the ridge waveguide structure was shown in the upper inset of Figure 18(a), where the upside of the

http://dx.doi.org/10.5772/60705

ridge was narrowed due to the lateral etching. For the devices fabricated by sample A, no lasing was observed even at 77 K and injected by current up to 1 A. For sample B, around 2.3 μm lasing was observed at low temperatures. This implies that the SCH is very crucial for the device performances, even more important than the crystalline quality of the QWs. For sample B the optical confinement factor is calculated about 0.22, but for sample A the confinement factor is only 0.12 because only the QWs provide a very limited optical confinement in sample A. Figure 18 shows the typical 77 K CW spectrum of the device fabricated by sample B injected by the current of 195 mA. The lasing was declined markedly as the temperature increases. The maximum operation temperature was about 100 K in CW mode and 170 K in pulsed mode with a 5% duty cycle. The lasing transition energy is close to the transition from $In_{0.8}Ga_{0.2}As$ waveguide layers, indicating that excessive band filling exists and higher gain from the QW transition is required. Quite a few carriers may escape from the QWs to the $In_{0.8}Ga_{0.2}As$ layers, due to the small offsets of conductive and valence bands between InAs and $In_{0.8}Ga_{0.2}As$ layers, especially when injected by relatively high currents. The 77 K I-V-P curves of sample B are shown in the lower inset of Figure 18(a). The output power was smaller than 1 mW/facet and the turn-on voltage was about 0.5 V.

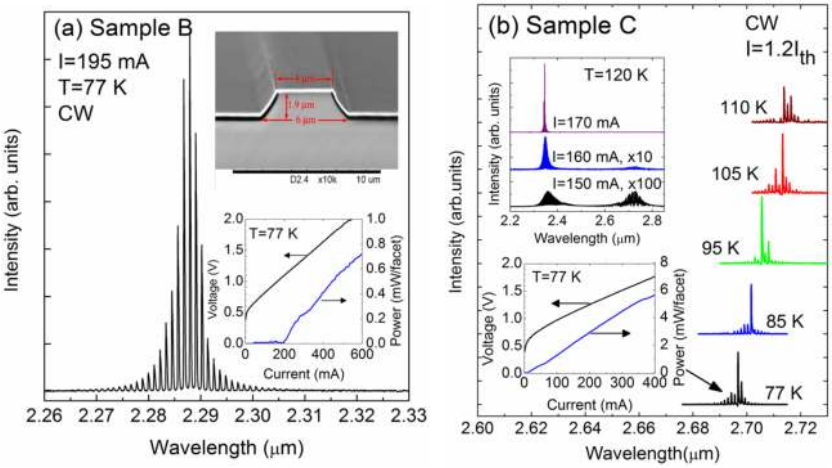

Figure 18. (a) CW lasing spectrum of sample B at 77 K. The upper inset shows the cross-section image of the ridge waveguide structure and the lower inset shows the I-V-P spectra of sample B at 77 K. (b) The temperature-dependent spectra of sample C. The upper inset shows the spectra at different injection currents at 120 K. The lower inset shows the I-V-P spectra at 77 K [55]. (Reprinted with permission from IOP)

For sample C, the CW lasing as long as 2.7 μm was observed, and the temperature-dependent lasing spectra are shown in Figure 18(b). The laser was operated in CW mode and injected by the current of 1.2 times the threshold current. As shown in the lower inset of Figure 18(b), the output power at 77 K was 5.7 mW/facet injected by the current of 400 mA and the turn-on voltage was about 0.65 V. The lasing wavelength moved from 2.70 μm at 77 K to above 2.71 μm at 110 K. When the temperature increased to 120 K, the lasing bounded to around 2.34 μm. The luminescence spectra at different injection currents at 120 K are shown in the upper inset of Figure 18(b). Two luminescence envelops at about 2.34 μm and 2.7 μm can be observed

under the injection current of 150 mA. As the injection current increased the 2.34 μm luminescence was enhanced whereas the 2.7 μm luminescence was declined, and only the lasing at 2.34 μm could be observed when the injection current was increased to 170 mA.

Sample C combines with SCH and strain-compensated QWs and shows the best performances in these three metamorphic QW laser structures. The calculated optical confinement factor of sample C is about 0.21, close to that of sample B with SCH. The larger bandgap of $In_{0.6}Ga_{0.4}As$ barrier layers compared to that of $In_{0.8}Ga_{0.2}As$ barriers in sample B can also enhance the carrier confinement and gain of QWs. On the other hand, the strain-compensated QWs ensure the feasible material quality. Nevertheless, the confinements in this laser structure are still unfavorable, as the bandgap of $In_{0.8}Ga_{0.2}As$ waveguide layers is smaller than that of $In_{0.6}Ga_{0.4}As$ barriers, and the refraction index is larger in $In_{0.8}Ga_{0.2}As$ waveguide. The excessive band filling carrier overflow still exists and the lasing at 2.34 μm is possibly due to the transition from the waveguide layers. Generally, increasing the QW number is an effective approach to improve the optical gain and confinement, but more QWs may introduce more strain in the QW region. The growth process needs to be optimized and a tradeoff needs to be considered between the material quality and the QW number.

6. Conclusion

In conclusion, we have demonstrated InP-based Sb-free QW lasers in 2-3 μm wavelength band by optimizing the structural design, GSMBE growth and device processing. To control the strain in the pseudomorphic QW region, the QWs with triangular shape were grown by using digital alloy technology. RT-CW lasers up to 2.43 μm have been successfully achieved by this approach and the performances are competitive to those well-developed GaSb-based QW lasers. Metamorphic InAs QWs were grown on InP-based $In_{0.8}Al_{0.2}As$ template to extend the lasing wavelength even longer. The lasers with CW lasing up to 2.71 μm have been demonstrated by applying 15 nm thick InAs QWs, although they still can only work at a low temperature of 110 K. Our efforts make clear that the extending of the lasing wavelength of InP-based Sb-free QW lasers into 2-3 μm band is not only attractive, but also practical. For CW operation of the laser at RT, the lasing wavelength up to about 2.5 μm should be possible through the fine design of the epitaxial structure, as well as optimization of the growth and processing technologies, adopting pseudomorphic or metamorphic schemes. For longer wavelengths, limited by the strain in pseudomorphic scheme or poor material quality and confinements of both photons and carriers in metamorphic scheme, the reachable performances of the lasers are degraded remarkably.

Acknowledgements

This work is supported by the National Basic Research Program of China under grant No. 2012CB619200 and the National Natural Science Foundation of China under grant Nos. 61275113, 61204133 and 61405232.

Author details

Yi Gu* and Yong-Gang Zhang

*Address all correspondence to: ygu@mail.sim.ac.cn

State Key Laboratory of Functional Materials for Informatics, Shanghai Institute of Microsystem and Information Technology, Chinese Academy of Sciences, China

References

[1] Lei W, Jagadish C. Lasers and photodetectors for mid-infrared 2-3 μm applications. J. Appl. Phys. 2008; 104(9), 091101.

[2] Tittel F K, Richter D, Fried A. Mid-infrared laser applications in spectroscopy. Topics Appl. Phys. 2003; 89, 445–516.

[3] Zhang Y G, Gu Y. Gas source MBE grown wavelength extending InGaAs photodetectors. In: Gian-Franco Dalla Betta (ed.) Advances in photodiodes. Rijeka: InTech; 2011. pp. 349–376.

[4] Dhar N K, Dat R, Sood A K. Advances in infrared detector array technology. In: Pyshkin S L, Ballato J M (ed.) Optoelectronics – Advanced materials and devices. Rijeka: InTech; 2013. pp. 149–190.

[5] Bleuel T, Müller M, Forchel A. 2-μm GaInSb-AlGaAsSb distributed-feedback lasers. IEEE Photon. Technol. Letts. 2001; 13(6), 553.

[6] Belenky G, Shterengas L, Kipshidze G, Hosoda T. Type-I diode lasers for spectral region above 3 μm. IEEE J. Select Top. Qutuantum Electron. 2011; 17, 1426.

[7] Sanchez D, Cerutti L, Tournie E. Single-mode monolithic GaSb vertical-cavity surface-emitting laser. Optics Express 2012; 20, 15540.

[8] Vizbaras K, Amann M C. Room-temperature 3.73 μm GaSb-based type-I quantum-well lasers with quinternary barriers. Semicond. Sci. Technol. 2012; 27, 032001.

[9] Zhang Y G, Li A Z, Zheng Y L, Lin C, Jian G Z. MBE grown 2.0 μm InGaAsSb/AlGaAsSb MQW ridge waveguide laser diodes. J. Cryst. Growth 2001; 227–228, 582–585.

[10] Zhang Y G, Zheng Y L, Lin C, Li A Z, Liu S. Continuous wave performance and tunability of MBE grown 2.1 μm InGaAsSb/AlGaAsSb MQW lasers. Chin. Phys. Lett. 2006; 23(8), 2262.

[11] Zhang Y G, Zhang X J, Zhu X R, Li A Z, Liu S. Tunable diode laser absorption spectroscopy detection of N_2O at 2.1 μm using antimonide laser and InGaAs photodiode. Chin. Phys. Lett. 2007; 24(8), 230.

[12] Zhang Y G, Gu Y, Zhang X J, Li A Z, Tian Z B. Gas sensor using a robust approach under time multiplexing scheme with a twin laser chip for absorption and reference. Chin. Phys. Lett. 2008; 25(9), 3246–3249.

[13] Baranov A N, Cuminal Y, Boissier G, Alibert C, Joullié A. Low-threshold laser diodes based on type-II GaInAsSb/GaSb quantum-wells operating at 2.36 μm at room temperature. Electron. Lett. 1996; 32, 2279.

[14] Rossner K, Hummer M, Lehnhardt T, Muller M, Forchel A, Fischer M, Koeth J. Continuous-wave operation of GaInAsSb/GaSb type-II ridge waveguide lasers emitting at 2.8 μm. IEEE Photon. Technol. Lett. 2006; 18(13), 1424.

[15] Yang R Q. Infrared laser based on intersubband transitions in quantum wells. Superlattices Microstruct. 1995; 17(1), 77.

[16] Sprengel S, Andrejew A, Vizbaras K, Gruendl T, Geiger K, Boehm G, Grasse C, Amann M C. Type-II InP-based lasers emitting at 2.55 μm. Appl. Phys. Lett. 2012; 100(4), 041109.

[17] Chang C H, Li Z L, Pan C H, Lu H T, Lee C P, Lin S D. Room-temperature mid-infrared "M"-type GaAsSb/InGaAs quantum well lasers on InP substrate. J. Appl. Phys. 2014; 115(6), 063104.

[18] Cornet C, Doré F, Ballestar A, Even J, Bertru N, Corre A, Loualiche S. InAsSb/InP quantum dots for midwave infrared emitters: A theoretical study. J. Appl. Phys. 2005; 98, 126105.

[19] Zhu C, Zhang Y G, Li A Z, Zheng Y L. Comparison of thermal characteristics of antimonide and phosphide MQW lasers. Semicond. Sci. Technol. 2005; 20, 563.

[20] Zhu C, Zhang Y G, Li A Z, Zheng Y L, Tang T. Heat management of MBE-grown antimonide lasers. J. Cryst. Growth 2005; 278, 173.

[21] Razeghi M, Bandyopadhyay N, Bai Y B, Lu Q Y, Slivken S. Recent advances in mid infrared (3–5 μm) quantum cascade lasers. Opt. Mater. Express 2013; 3(11), 1872.

[22] Vurgaftman I, Meyer J R, Ram-Mohan L R. Band parameters for III–V compound semiconductors and their alloys. J. Appl. Phys. 2001; 89, 5815.

[23] Zhang Y G, Chen J X, Chen Y Q, Qi M, Li A Z, Frojdh K, Stoltz B. Characteristics of strain compensated 1.3 μm InAsP/InGaAsP ridge waveguide laser diodes grown by gas source MBE. J. Cryst. Growth 2001; 227–228, 329–333.

[24] Forouhar S, Ksendzov A, Larsson A, Temkin H. InGaAs/InGaAsP/InP strained layer quantum well lasers at ~2 μm. Electron. Lett. 1992; 28(15), 1431.

[25] Forouhar S, Keo S, Larsson A, Ksendzov A, Temkin H. Low threshold continuous operation of InGaAs/InGaAsP quantum well lasers at ~2.0 μm. Electron. Lett. 1993; 29(7), 574.

[26] Major J S, Nam D W, Osinski J S, Welch D F. High-power 2.0 μm InGaAsP laser diodes. IEEE Photon. Technol. Lett. 1993; 5(6), 594.

[27] Martinelli R U, Menna R J, Triano A, Harvey M G, Olsen G H. Temperature dependence of 2 μm strained-quantum-well InGaAs/InGaAsP/InP diode lasers. Electron. Lett. 1994; 30(4), 324.

[28] Ochiai M, Temkin H, Forouhar S, Logan R A. InGaAs-InGaAsP buried heterostructure lasers operating at 2.0 μm. IEEE Photon. Technol. Lett. 1995; 7(8), 825.

[29] Oishi M, Yamamoto M, Kasaya K. 2.0-μm single-mode operation of InGaAs-InGaAsP distributed-feedback buried-heterostructure quantum-well lasers. IEEE Photon. Technol. Lett. 1997; 9(4), 431.

[30] Mitsuhara M, Ogasawara M, Oishi M, Sugiura H. 2.05-μm wavelength InGaAs-InGaAs distributed-feedback multiquantum-well lasers with 10-mW output power. IEEE Photon. Technol. Lett. 1999; 11(1), 33.

[31] Mitsuhara M, Ogasawara M, Oishi M, Sugiura H. Metalorganic molecular-beam-epitaxy-grown $In_{0.77}Ga_{0.23}As$/InGaAs multiple quantum well lasers emitting at 2.07 μm wavelength. Appl. Phys. Lett. 1998; 72(24), 3106.

[32] Kuang G K, Böhm G, Grau M, Rösel G, Meyer R, Amann M C. 2.12 μm InGaAs-InGaAlAs-InP diode lasers grown in solid-source-molecular-beam epitaxy. Appl. Phys. Lett. 2000; 77(8), 1091.

[33] Ortsiefer M, Böhm G, Grau M, Windhorn K, Rönneberg E, Rosskopf J, Shau R, Dier O, Amann M C. Electrically pumped room temperature CW VCSELs with 2.3 μm emission wavelength. Electron. Lett. 2006; 42(11), 640.

[34] Boehm G, Grau M, Dier O, Windhorn K, Roenneberg E, Rosskopf J, Shau R, Meyer R, Ortsiefer M, Amann M C, Growth of InAs-containing quantum wells for InP-based VCSELs emitting at 2.3 μm. J. Cryst. Growth. 2007; 301–302, 941–944.

[35] Sato T, Mitsuhara M, Kondo Y. 2.33 μm-wavelength InAs/InGaAs multiple-quantum-well lasers grown by MOVPE. Electron. Lett. 2007; 43(21), 1143.

[36] Sato T, Mitsuhara M, Nunoya N, Kasaya K, Kano F, Kondo Y. 2.33-μm-wavelength distributed feedback lasers with InAs-$In_{0.53}Ga_{0.47}As$ multiple-quantum wells on InP substrates. IEEE Photon. Technol. Lett. 2008; 20(12), 1045.

[37] Sato T, Mitsuhara M, Kakitsuka T, Fujisawa T, Kondo Y. Metalorganic vapor phase epitaxial growth of InAs/InGaAs multiple quantum well structures on InP substrates. IEEE J. Sel. Topics Quan. Electron. 2008; 14(4), 992.

[38] Gu Y, Zhang Y G, Cao Y Y, Zhou L, Chen X Y, Li Hsby, Xi S P. 2.4-μm InP-based antimony-free triangular quantum well lasers in continuous-wave operation above room temperature. Appl. Phys. Express 2014; 7, 032701.

[39] Krier A, Chubb D, Krier S E, Hopkinson M, Hill G. Light sources for wavelengths >2 μm grown by MBE on InP using a strain relaxed buffer. IEE Proc. 1998; 145(5), 292.

[40] Kirch J, Garrod T, Kim S, Park J H, Shin J C, Mawst L J, Kuech T F, Song X, Babcock S E, Vurgaftman I, Meyer J R, Kuan T S. $InAs_yP_{1-y}$ metamorphic buffer layers on InP substrates for mid-IR diode lasers. J. Cryst. Growth 2010; 312, 1165–1169.

[41] Jung D, Song Y, Yu L, Wasserman D, Lee M L. 2.8 μm emission from type-I quantum wells grown on InAsP/InP metamorphic graded buffer. Appl. Phys. Lett. 2012; 101, 251107.

[42] Gu Y, Zhang Y G, Wang K, Fang X, Li C, Cao Y Y, Li A Z, Li Y Y. InP-based InAs/InGaAs quantum wells with type-I emission beyond 3 μm. Appl. Phys. Lett. 2011; 99, 081914.

[43] Cao Y Y, Zhang Y G, Gu Y, Chen X Y, Zhou L, Li Hsby. 2.7 μm InAs quantum well lasers on InP-based InAlAs metamorphic buffer layers. Appl. Phys. Lett. 2013; 102, 201111.

[44] Gu Y, Zhang Y G, Chen X Y, Cao Y Y, Fang X, Ding G Q, Zhou L. InAs/$In_{0.83}Al_{0.17}As$ quantum wells on GaAs substrate with type-I emission at 2.9 μm. Appl. Phys. Lett. 2013; 102, 121110.

[45] Gu Y, Zhang Y G, Liu S. Strain compensated AlInGaAs/InGaAs/InAs triangular quantum wells for lasing wavelength beyond 2 μm. Chin. Phys. Lett. 2007; 24, 3237–3240.

[46] Gu Y, Zhang Y G. Properties of strain compensated symmetrical triangular quantum wells composed of InGaAs/InAs chirped superlattice grown using gas source molecular beam epitaxy. Chin. Phys. Lett. 2008; 25, 726–729.

[47] Chen J X, Li A Z, Chen Y Q, Guo F M, Lin C, Zhang Y G, Qi M. Quasi RT-CW operation of InGaAs/InGaAsP strained quantum well lasers. J. Cryst. Growth 2001; 227–228, 338–342.

[48] Gu Y, Zhang Y G, Wang K, Li A Z, Li Y Y. Optimization of AlInGaAs/InGaAs/InAs strain compensated triangular quantum wells grown by gas source molecular beam epitaxy for laser applications in 2.1–2.4 μm range. J. Cryst. Growth 2009; 311, 1935–1938.

[49] Giugni S, Tansley T L, Green F, Shwe C, Gal M. Optical transitions in symmetric, compositionally graded triangular AlGaAs quantum wells grown by molecular beam epitaxy. J. Appl. Phys. 1992; 71, 3486–3491.

[50] Lin D Y, Lin F C, Huang Y S, Qiang H, Pollak Fred H, Mathine D L, Maracas G N. Piezoreflectance and photoreflectance study of GaAs/AlGaAs digital alloy compositional graded structures. J. Appl. Phys. 1996; 79, 460–466.

[51] Jourba S, Gendry M, Marty O, Pitaval M, Hollinger G. High-quality highly strained InGaAs quantum wells grown on InP using $(InAs)_n(GaAs)_{0.25}$ fractional monolayer superlattices. Appl. Phys. Lett. 1999; 75, 220.

[52] Cao Y Y, Zhang Y G, Gu Y, Chen X Y, Zhou L, Li Hsby. Improved performance of 2.2 μm InAs/InGaAs QW lasers on InP by using triangular wells. IEEE Photon. Technol. Lett. 2014; 26(6), 571–574.

[53] Gu Y, Wang K, Li Y Y, Li C, Zhang Y G. InP-based InGaAs/InAlGaAs digital alloy quantum well laser structure at 2 μm. Chin. Phys. B 2010; 19, 077304.

[54] Cao Y Y, Gu Y, Zhang Y G, Li Y Y, Fang X, Li A Z, Zhou L, Li Hsby. InAs/InGaAs digital alloy strain-compensated quantum well lasers. J. Infrared Millim. Waves 2014; 33(3), 213–217.

[55] Gu Y, Chen X Y, Zhang Y G, Cao Y Y, Fang X, Li Hsby. Type-I mid-infrared InAs/InGaAs quantum well lasers on InP-based metamorphic InAlAs buffers. J. Phys. D: Appl. Phys. 2013; 46, 505103.